Journal of CO2 Utilization 105 (2026) 103356

Contents lists available at ScienceDirect

Journal of CO2 Utilization

journal homepage: www.elsevier.com/locate/jcou

Ferrocene-linked triazine-based porous organic polymers as multifunctional platforms for CO_2 recognition, separation and utilization

Mohamed Gamal Mohamed [a,b], Wei-Chun Huang [a], Mohsin Ejaz [a], Yang-Chin Kao [a], Yen-Min Lo [a], Ahmed A.K. Mohammed [b], Yen-Ling Kuan [a], Shiao-Wei Kuo [a,c,*]

[a] Department of Materials and Optoelectronic Science, Center for Functional Polymers and Supramolecular Materials, National Sun Yat-Sen University, Kaohsiung 804, Taiwan
[b] Chemistry Department, Faculty of Science, Assiut University, Assiut 71515, Egypt
[c] Department of Medicinal and Applied Chemistry, Kaohsiung Medical University, Kaohsiung 807, Taiwan

ARTICLE INFO

Keywords:
Ferrocene
Triazine
Porous organic polymer
CO_2 capture
Cyclic carbonates

ABSTRACT

The development of efficient materials that can capture CO_2 and catalyze its conversion into value-added organic compounds is critically important. The concept of CO_2 Capture and Utilization (CCU) is gradually gaining the attention of researchers. In this study, we designed and synthesized ferrocene and triazine-based porous organic polymers (POP), named FC-TPT-POP and FC-TPT-Ph-POP, through a Schiff base reaction for CO_2 capture, and utilized them as catalysts to transform CO_2 and various epoxides into cyclic carbonates via a cycloaddition process. The FC-TPT-POP showed high surface area (797 m^2 g^{-1}) and microporosity. The presence of high surface area, porosity, and triazine units having nitrogen basic sites showed excellent selective CO_2 capture (3.34 mmol g^{-1} at 1 bar pressure/273 K, Q_{st} of 34 kJ mol^{-1}). Both POPs show strong CO_2 selectivity at low pressures due to interactions between nitrogen sites and the highly polar, high-quadrupole CO_2 molecules. FC-TPT-POP outperforms FC-TPT-Ph-POP, achieving a CO_2/N_2 selectivity of about 40 at 273 K. Moreover, it demonstrates outstanding catalytic performance in transforming simple terminal epoxides into cyclic carbonates using CO_2 as a reactant. For example, under mild conditions (120 °C, 400 psi, 8 h), FC-TPT-POP achieved a high conversion of 99.5 % toward propylene oxide (PO). The catalytic effect arises from the synergistic interaction of Lewis basic nitrogen atoms in the triazine units and the metal active sites of ferrocene. Therefore, the development of ferrocene-triazine-based POP catalysts in this study offers a promising strategy for lowering atmospheric CO_2 levels through efficient capture and catalytic conversion.

1. Introduction

In recent decades, the rapid pace of industrialization and human development has led to a sharp rise in greenhouse gas concentrations, particularly carbon dioxide (CO_2), in the atmosphere [1–3]. Among various greenhouse gases, CO_2 is a major contributor to global environmental concerns. Its increasing levels are primarily driven by the burning of fossil fuels and the growing global population, along with natural sources such as wildfires and biomass burning [4–7]. This steady escalation in CO_2 levels is linked to serious environmental challenges, including global warming, ocean acidification, and climate change, highlighting the urgency of climate mitigation efforts [8,9]. One of the most promising strategies to combat rising CO_2 levels is carbon capture and utilization (CCU) [10–13]. This approach not only involves separating CO_2 from emission sources but also converting it into the value-added chemicals [14,15]. The selective capture of CO_2 from complex gas mixtures remains a critical step in this process. Various techniques have been explored for this purpose, including chemical absorption [16], membrane filtration [17], adsorption [18], and cryogenic separation [19]. In recent years, the use of CO_2 as a renewable carbon source for synthesizing useful chemical products has gained significant momentum. However, thermodynamic stability and strong molecular bonds of CO_2 make it chemically inert and difficult to act under mild conditions. Overcoming this challenge requires the development of efficient, low-cost catalysts that can operate under moderate reaction conditions. Among several CO_2 transformation routes, the

* Corresponding author at: Department of Materials and Optoelectronic Science, Center for Functional Polymers and Supramolecular Materials, National Sun Yat-Sen University, Kaohsiung 804, Taiwan.
E-mail address: kuosw@faculty.nsysu.edu.tw (S.-W. Kuo).

https://doi.org/10.1016/j.jcou.2026.103356
Received 22 August 2025; Received in revised form 4 January 2026; Accepted 5 February 2026
Available online 10 February 2026

process of reacting CO_2 with epoxides to synthesize cyclic carbonates has emerged as an attractive option [20–24]. Cyclic carbonates are valuable intermediates that find wide application as lithium-ion battery electrolytes, environmentally friendly solvents [25,26], and as precursors for the synthesis of aliphatic and aromatic polycarbonates as well as polyhydroxyurethanes [27–29]. Yet, the inherent kinetic and thermodynamic stability of CO_2 continues to limit its reactivity in most catalytic systems.

To facilitate CO_2 conversion, researchers are actively seeking catalysts that can promote the efficient formation of cyclic carbonates from epoxides. Porous materials have emerged as strong candidates for this purpose due to their high surface areas and the possibility of introducing surface-active basic sites [30–34]. These materials have been broadly explored for their applicability in chemical sensing, gas separation, heterogeneous catalysis, and energy storage [35–39]. Precursors such as zeolites, metal-organic frameworks (MOFs), porous carbons, and especially porous organic polymers (POPs) have shown promise in CO_2 capture and conversion technologies [40–43]. In POPs, and MOFs, the nature of the building blocks determines the pore architecture and the chemical environment within the pores. Since CO_2 is a linear, non-polar molecule with a strong quadrupole moment, surface modifications involving electron-donating or electron-withdrawing groups (such as N, O, P, S, or F) can enhance its interactions with the adsorbent through dipole–quadrupole interactions [44–47]. POPs have drawn substantial focus owing to their tunable porosity and chemical versatility. Their modular design allows for meticulous adjustment of the structure and functionalization, enabling the development of materials tailored for gas storage, separation, and catalysis [48]. POPs containing basic functional groups are especially attractive for CO_2-related applications, as they can serve both as adsorbents and as catalytic platforms. To further enhance their performance, POPs designed with Lewis or Brønsted acid sites, along with high densities of CO_2-philic functional groups, offer an integrated solution for both CO_2 capture and conversion [49]. However, challenges remain in optimizing their electronic properties and catalytic efficiency for CO_2 transformation [50]. Continued innovation in POPs design is essential to develop multifunctional systems capable of efficient and sustainable CO_2 utilization. Liu et al. showed that the SCTF-CF_3/KI catalyst achieves 96 % yield and 99 % selectivity for converting low-concentration CO_2 to bromopropene carbonate in a metal- and solvent-free process [51]. They also developed durable TCTB@Zn-iCOPs for efficient CO_2 cycloaddition to cyclic carbonates [52]. The high-surface-area, pyridine-rich polymer TPA-HCP-Py (1133 m^2 g^{-1}) can capture and convert atmospheric CO_2 to cyclic carbonates with good yields and recyclability [53].

To address this challenge, we strategically incorporated two representative functional units, triazine and ferrocene into the POP frameworks. Triazine, with its nitrogen-rich structure and lone electron pairs, serves as an excellent electron-donating group. These lone pairs facilitate transient electronic interactions with electrophilic species such as CO_2, making triazine an ideal component for gas capture [54–56]. Ferrocene, a well-known organometallic compound, consists of a divalent iron center (Fe^{2+}) sandwiched between two cyclopentadienyl (Cp^-) rings, forming a stable, symmetric sandwich structure. Its aromatic stability and ease of functionalization make it a versatile building block for porous material design [57–59]. To synergize the benefits of these two functional moieties, we covalently linked triazine and ferrocene-based building blocks via Schiff base condensation, yielding two novel POPs: FC-TPT-POP and FC-TPT-Ph-POP. The key building blocks used were 1,1′-diacetylferrocene (DAFC), 4,4',4''-(1,3,5-triazine-2,4,6-triyl)trianiline (TPT-3NH_2), and 4′,4‴,4⁗-(1,3,5-triazine-2,4,6-triyl)tris(([1,1′-biphenyl]-4-amine)) (TPT-Ph-3NH_2). To the best of our knowledge, the combination of DAFC with TPT-3NH_2 or TPT-Ph-3NH_2 to construct POPs for CO_2 capture and utilization has not been previously reported. The incorporation of ferrocene into the POP backbone introduces bifunctional catalytic sites. The iron centers act as a Lewis acid sites to activate epoxides, while the organic framework provides complementary CO_2 philic domains. This dual-function architecture enables synergistic interactions between the gas molecules and active sites, thereby enhancing the overall catalytic performance. Our study focuses on the cycloaddition of CO_2 with epoxide compounds to yield cyclic carbonates value-added cyclic carbonates, which have broad applications in lithium battery electrolytes, green solvents, and polymer precursors. Additionally, due to the insolubility of POPs in most solvents, they serve as robust, reusable heterogeneous catalysts. They can be easily recovered through simple rinsing, demonstrating excellent recyclability and supporting the principles of green chemistry and sustainable development.

2. Experimental section

2.1. Materials

Trifluoromethanesulfonic acid (TFMS), bis(cyclopentadienyl) iron 99 % (ferrocene, FC) from Sigma-Aldrich. 4-Aminobenzonitrile (4-aminoBZCN), and 4′-amino-[1,1′-biphenyl]-4-carbonitrile (4-aminoBPCN) from Matrix Scientific. Dimethyl sulfoxide (DMSO), acetyl chloride (CH_3COCl), dichloromethane (CH_2Cl_2), propylene oxide (PO), *tert*-butyl glycidyl ether (*t*-BGE), cyclohexane oxide (CHO), 2-Ethylhexyl glycidyl ether (EHGE), and phenyl glycidyl ether (PGE) from Acros Organics. Bis(triphenylphosphoranylidene)ammonium chloride (PPNCL) from TCI. Aluminum chloride ($AlCl_3$) from Showa. The schematic synthesis routes for 1,1′-diacetylferrocene (DAFC), TPT-3NH_2, and TPT-Ph-3NH_2 are illustrated in Schemes S1–S3, while their corresponding spectroscopic data, including ^1H and ^{13}C NMR, are provided in Figs. S1 and S2 [32,60–62].

2.2. Synthesis of FC-TPT-POP and FC-TPT-Ph-POP

A mixture of DAFC (0.45 g, 1.65 mmol) and either TPT-3NH_2 (0.294 g, 0.81 mmol) or TPT-Ph-3NH_2 (0.48 g, 0.81 mmol) was put into a glass container containing 50 mL of DMSO. The temperature of the reaction mixture increased to 180 °C and was stirred under a nitrogen atmosphere for approximately three days. After completion, the reaction was cooled to RT, resulting in the formation of a black solid, which was collected by filtration. The crude product was purified through Soxhlet extraction using THF, chloroform, methanol, and acetone in sequence. The final product, either FC-TPT-POP or FC-TPT-Ph-POP, was dried at 120 °C to yield fine black powder [Scheme 1]. Elemental analysis (EA) for FC-TPT-POP: C (71.07 %), H (6.67 %), and N (10.32 %). EA for FC-TPT-Ph-POP: C (83.71 %), H (5.94 %), and N (8.24 %). The Fe content of Py-FC-TPT-POP and FC-TPT-Ph-POP was determined by inductively coupled plasma mass spectrometry (ICP-MS) analysis to be 2.3821 wt% and 2.3025 wt%, respectively.

2.3. Catalytic CO_2 utilization performance of POPs

To evaluate the catalytic potential of POPs in CO_2 utilization reactions, a high-pressure reactor system was employed to facilitate the cycloaddition of various epoxides, such as PO, *t*-BGE, CHO, EHGE, and PGE, with CO_2 to produce the value-added cyclic carbonates. POPs were used as the primary catalysts, while PPNCl was introduced as an anionic catalyst to enhance both catalytic activity and selectivity. The reactions were carried out in a stainless-steel autoclave at a constant CO_2 pressure of 400 psi and a temperature of 120 °C. Both the POP catalyst and PPNCl were used in equal amounts (50 mg each), and the quantity of each epoxide monomer was adjusted to maintain a catalyst to monomer molar ratio of 1:820. This setup effectively mimics industrial conditions, enabling a realistic evaluation of the catalytic efficiency for CO_2 conversion.

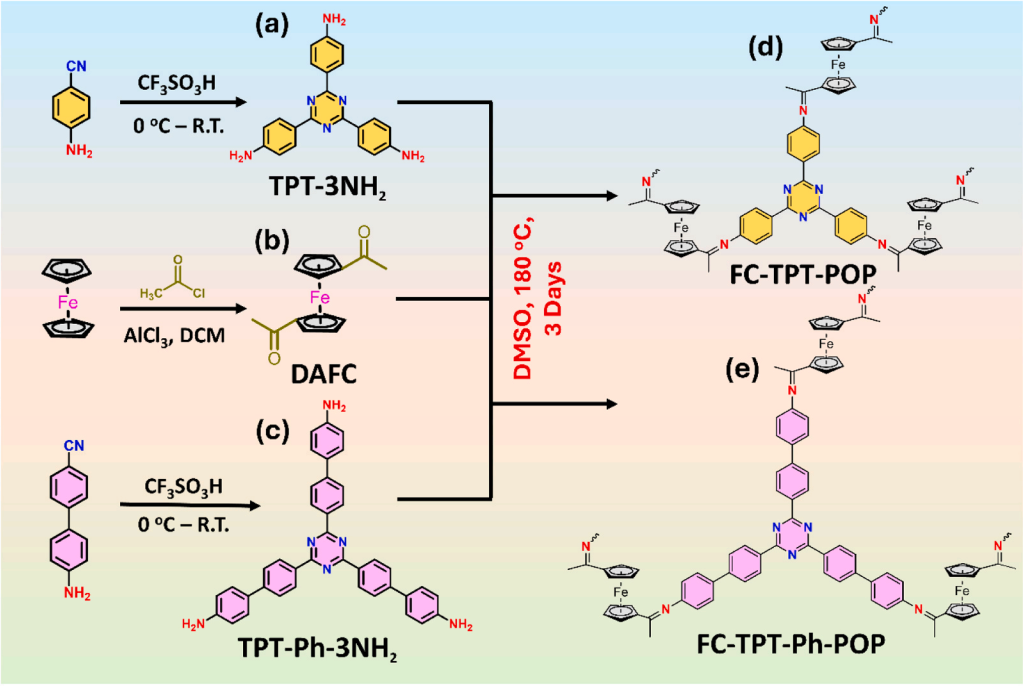

Scheme 1. Synthesis routes of (a) TPT-3NH_2, (b) DAFC, (c) TPT-Ph-3NH_2, (d) FC-TPT-POP, and (e) FC-TPT-Ph-POP.

3. Results and discussion

3.1. Synthesis and characterization of FC-TPT-POP and FC-TPT-Ph-POP

The target amine-functionalized monomers, TPT-3NH_2 and TPT-Ph-3NH_2, were synthesized via the reaction of 4-aminoBZCN and 4-aminoBPCN, respectively, with TMSA at 0 °C for 24 h [Schemes 1**(a) and** 1**(c)**]. Subsequently, DAFC was obtained by the acetylation of FC using CH_3COCl in the presence of $AlCl_3$ as a Lewis acid catalyst [Scheme 1**(b)**]. Finally, the FC-TPT-POP [Scheme 1**(d)**] and FC-TPT-Ph-POP [Scheme 1 **(e)**] were constructed via the condensation of DAFC with TPT-3NH_2 and TPT-Ph-3NH_2, respectively, in DMSO as the reaction medium. The synthesis of FC-TPT-POP and FC-TPT-Ph-POP was confirmed by FTIR NMR, and XPS spectroscopy. In the FTIR spectrum, the ferrocene monomer exhibited a distinct C═O stretching absorption band at approximately 1660 cm^{-1}, while the NH_2 groups in TPT and TPT-Ph showed characteristic N–H stretching vibrations in the range of 3300–3450 cm^{-1} [Figs. S3(a) and S3(b)]. After polymerization to form FC-TPT-POP and FC-TPT-Ph-POP, these C═O and NH_2 signals disappeared, and a new absorption band emerged at around 1650 cm^{-1}, corresponding to the imine (C═N) stretching vibration, strong evidence of the successful Schiff base condensation reaction, resulting formation of the FC-TPT-POP and FC-TPT-Ph-POP networks [Fig. 1**(b) and** Figs. S3 (a) and S3(b)]. The characteristic vibrational bands associated with the triazine framework, including the C═N and C-N observed at 1513 and 1362 cm^{-1}, respectively [Fig. 1**(b)**]. Additionally, the presence of the C–H stretching band on the ferrocene ring at approximately 1014 cm^{-1} further confirms that the structural backbone of the monomers remained intact throughout the polymerization process [Fig. 1**(b)**]. Moreover, broad peaks detected in the range of 3300–3450 cm^{-1} in the FTIR spectra of both FC-TPT-POP and FC-TPT-Ph-POP are likely associated with the –OH stretching vibrations of water molecules entrapped within the porous frameworks [63]. These results collectively confirm the successful synthesis of the imine-linked POPs, retaining the key structural characteristics of both the ferrocene and triazine monomers. To further validate the Schiff base condensation reaction, solid-state ^{13}C NMR spectroscopy was conducted [Fig. 1**(c)**]. The ferrocene exhibited a distinct carbonyl carbon signal (C═O) at approximately 201 ppm, along with characteristic cyclopentadienyl ring carbon signals between 70–80 ppm [Fig. 1**(c) and** Figs. S3(c) and S3(d)]. The monomers of TPT-3NH_2 and TPT-Ph-3NH_2 both showed a clear C═N signal around 171 ppm, corresponding to the carbon atoms in the triazine ring [Figs. S3 (c) and S3(d)]. In addition, multiple aromatic carbon signals appeared in the 110–150 ppm region [Figs. S3 (c) and S3(d)], the TPT-Ph-3NH_2 showing a higher density and slightly upfield-shifted signals due to the additional phenyl ring in its structure. The ^{13}C NMR spectra of FC-TPT-POP and FC-TPT-Ph-POP showed the disappearance of the original C═O signal, accompanied by the emergence of a new C═N imine signal at approximately 180 ppm, clearly indicating the formation of imine linkages through Schiff base condensation [Fig. 1**(c) and** Figs. S3(c) and S3(d)]. Furthermore, both POPs retained the aromatic carbon signals from TPT or TPT-Ph, as well as the cyclopentadienyl (Cp) carbon signals of ferrocene, between 68.34 and 79.12 ppm, suggesting that the structural integrity of the monomeric building blocks was preserved during polymerization [61,62,64]. To investigate the thermal stability of the FC-TPT-POP and FC-TPT-Ph-POP, thermogravimetric analysis (TGA) was conducted in a N_2 environment, and the temperature was increased from room temperature to 800 °C [Fig. 1**(d)**]. Both FC-TPT-POP and FC-TPT-Ph-POP demonstrated significant thermal stability. The FC-TPT-POP showed T_{d5} at 237 °C, T_{d10} at 303 °C and a char yield of 60 wt%, while the FC-TPT-Ph-POP exhibited T_{d5} at 234 °C, T_{d10} at 304 °C and a char yield of 63 wt%, respectively [Table S1]. The FC-TPT-Ph-POP showed slightly better thermal stability than FC-TPT-POP, which can be attributed to the increased rigidity provided by the biphenyl spacer. These features make FC-TPT-POP and FC-TPT-Ph-POP promising candidates for high-temperature applications, such as gas capacity and heterogeneous catalysis. The crystallinity of FC-TPT-POP and FC-TPT-Ph-POP was investigated by powder X-ray diffraction (PXRD) analysis. Both FC-TPT-POP and FC-TPT-Ph-POP exhibit broad diffraction patterns without any distinct sharp peaks [Fig. S4]. A broad hump appearing in the 2θ range of approximately 18–25° indicates the presence of an amorphous structure. Such broad features are typically associated with disordered stacking, π–π interactions, or short-range ordering, which are commonly found in organic polymeric frameworks [65]. The slightly stronger intensity observed in FC-TPT-POP may indicate a more compact or ordered

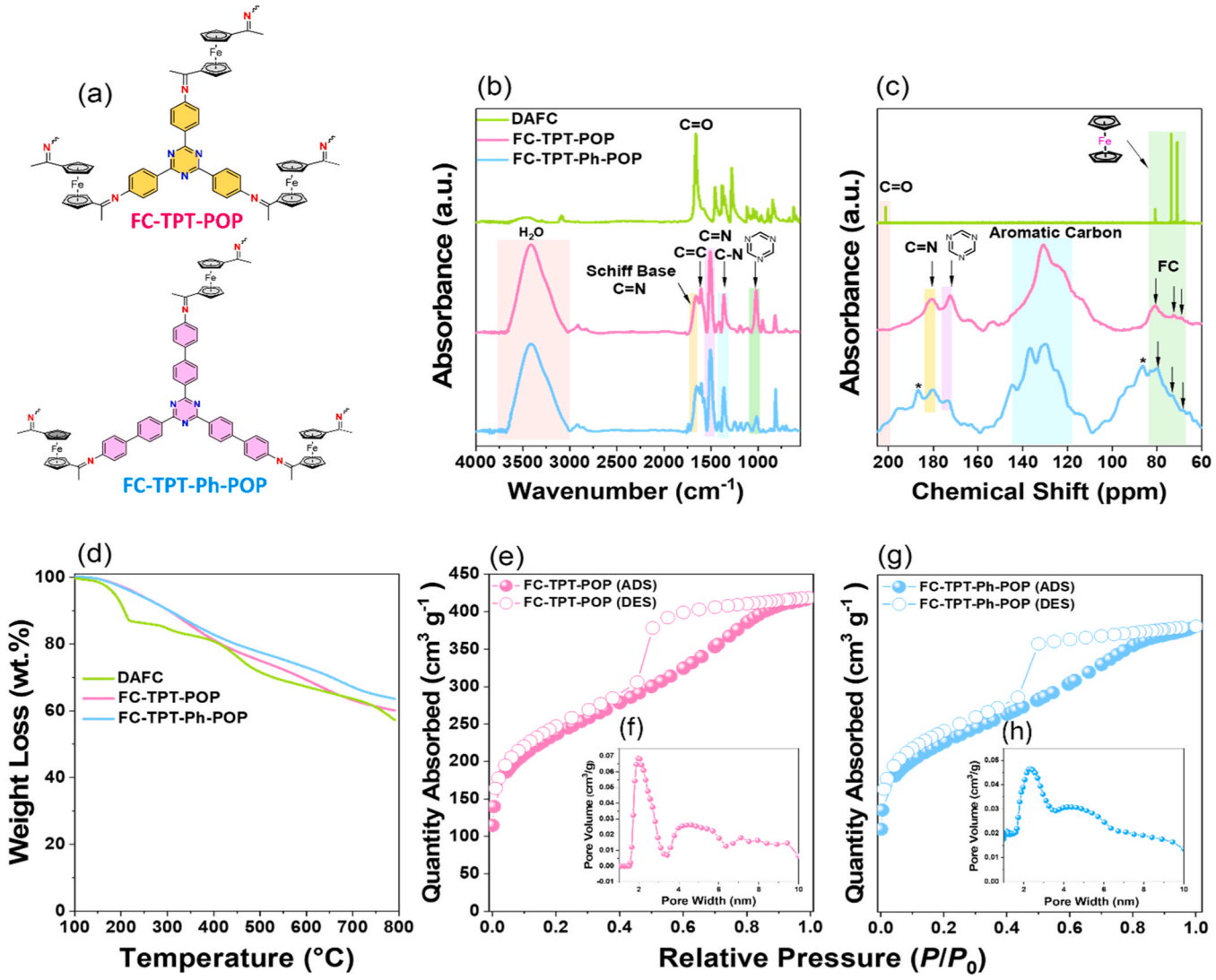

Fig. 1. (a) Molecular structures of FC-TPT-POP and FC-TPT-Ph-POP. (b) FTIR, (c) solid state ^{13}C NMR, and (d) TGA of FC-TPT-POP and FC-TPT-Ph-POP. (e, g) N_2 adsorption/desorption profiles and (f, h) pore size diameters of (e, f) FC-TPT-POP and (g, h) FC-TPT-Ph-POP.

stacking arrangement within the polymer backbone. In contrast, FC-TPT-Ph-POP, which incorporates bulky biphenyl moieties, likely experiences greater steric hindrance during polymerization, leading to reduced stacking regularity and consequently a weaker diffraction signal.

Overall, these PXRD results confirm that both POPS are amorphous. To evaluate the porosity and specific surface area of the FC-TPT-POP and FC-TPT-Ph-POP, N_2 adsorption/desorption isotherm measurements were conducted and analyzed using the Brunauer-Emmett-Teller (BET) model. Both POPs exhibit typical Type IV isotherms as defined by IUPAC [Figs. 1**(e) and 1(g)**]. A notable feature is the presence of a clear hysteresis loop in the medium relative pressure range ($P/P_0 \approx 0.4$–0.9), indicating that the desorption process occurs at different pressures and rates compared to adsorption. This behavior is commonly observed in materials with hierarchical micro- and mesoporous structures, particularly those with slit-shaped pores or ink bottle-type pore geometries [66]. The pore size distribution curves further support this observation. Both samples exhibit pore diameters mainly in the range of 1.5–3.5 nm, spanning the boundary between micropores and mesopores, indicating the presence of well-developed hierarchical porosity [Figs. 1**(f) and 1(h)**]. Notably, FC-TPT-POP displays a higher adsorption capacity with a BET surface area of 797 $m^2\ g^{-1,}$ while FC-TPT-Ph-POP shows slightly lower adsorption capacity, with a BET surface area of 756 $m^2\ g^{-1}$ [Figs. 1**(e) and 1(g)**]. Further analysis of the pore size distribution reveals that FC-TPT-POP exhibits a sharp and symmetric peak centered at approximately 1.9 nm, indicating a narrow and uniform pore size distribution, suggesting well-controlled pore formation and high structural uniformity during the polymerization process. The FC-TPT-Ph-POP shows a broader distribution, with pore sizes mainly in the range of 2.5–3.5 nm [Table S1]. The signal is flatter and the peak shape less defined, suggesting a more heterogeneous pore size distribution and a slightly less ordered structure. This may be attributed to the steric hindrance introduced by the biphenyl units, which could partially limit pore development during polymerization. Nevertheless, the material retains a mesoporous nature with good pore volume and openness, making it suitable for gas adsorption and diffusion applications. To verify the elemental composition of the synthesized FC-TPT-POP and FC-TPT-Ph-POP, X-ray photoelectron spectroscopy (XPS) analysis was performed [Figs. 2**(a) and 2(e)**]. The signals corresponding to C 1s (~284 eV), N 1s (~400 eV), and Fe 2p (~710 eV) are observed in both POP, confirming the successful incorporation of the intended elements carbon, nitrogen, and iron into the polymer frameworks. In addition, the O 1s signal (~532 eV) is also detected, attributed to adsorbed atmospheric moisture or CO_2, and possibly minor surface oxidation of iron species or instrumental background noise, which are commonly observed in XPS measurements of porous materials [67]. Therefore, the

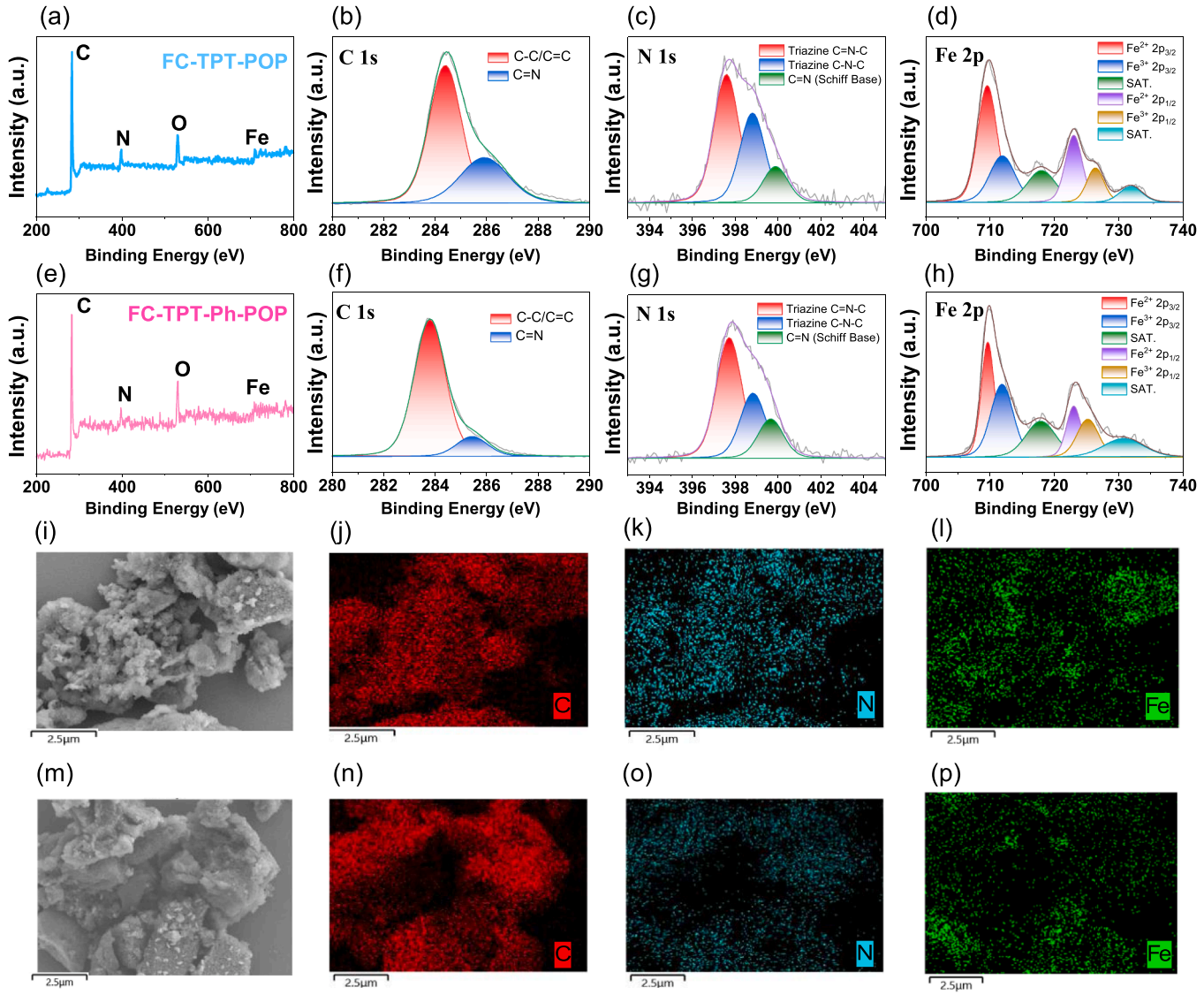

Fig. 2. XPS spectra of (a) FC-TPT-POP, (e) FC-TPT-Ph-POP, along with the corresponding high-resolution fits for (b, f) C 1s, (c, g) N 1s, and (d, h) Fe 2p in (b–d) FC-TPT-POP and (f–h) FC-TPT-Ph-POP. (i, m) SEM images and (j–p) SEM-EDS mapping images [C, N, and Fe] of (i–l) FC-TPT-POP, (m–p) FC-TPT-Ph-POP.

presence of oxygen is not considered an intrinsic component of the POPs structures. We further conducted high-resolution XPS fitting analysis focusing on the C 1s, N 1s, and Fe 2p, regions to investigate the detailed bonding environments of the elements present in FC-TPT-POP and FC-TPT-Ph-POP [Figs. 2**(d) and** 2**(h)]**. In the C 1s region, both POPs exhibit a major peak centered at approximately 284.5 eV, which corresponds to C–C/C═C bonds originating from aromatic rings and the cyclopentadienyl units of ferrocene [Figs. 2**(b) and** 2**(f)**]. In addition, a distinct peak observed at around 285.9 eV is assigned to C═N bonding, stemming from both the imine linkages formed via Schiff base condensation and the internal C═N bonds within the triazine rings. The N 1 s spectra of both POPs exhibit three well-resolved peaks located at approximately 397.7 eV, 398.8 eV, and 399.6 eV, which are attributed to C═N–C and C–N–C bonds within the triazine rings, as well as C═N imine bonds [Figs. 2**(c) and** 2**(g)**]. These results confirm the successful integration of both triazine and imine functionalities, indicating that the resulting POPs are rich in nitrogen, that are advantageous for gas adsorption and catalytic applications. In the Fe 2p region, both FC-TPT-POP and FC-TPT-Ph-POP display the characteristic spin-orbit doublet of Fe. Moreover, the FC-TPT-POP shows the Fe^{2+} $2p_{3/2}$ and Fe^{2+} $2p_{1/2}$ signals at 709.5 eV and 722.7 eV, and Fe^{3+} $2p_{3/2}$ and Fe^{3+} $2p_{1/2}$ signals at 711.5 eV and 726.2 eV, respectively. For the FC-TPT-Ph-POP, the corresponding Fe^{2+} $2p_{3/2}$ and Fe^{2+} $2p_{1/2}$ peaks appear at 709.8 eV and 722.9 eV, and Fe^{3+} $2p_{3/2}$ and Fe^{3+} $2p_{1/2}$ signals at 711.8 eV and 725.0 eV, respectively [Figs. 2**(d) and** 2**(h)]**. These features support the presence of ferrocene-derived iron atoms exhibiting mixed valence states in the porous network. To further confirm the spatial distribution of elements within POPs, field-emission scanning electron microscopy (FE-SEM) combined with energy-dispersive X-ray spectroscopy (EDS) was conducted, as presented in Fig. 2**(i–p)**.

The SEM images reveal aggregated particle morphology with a rough surface texture. Additionally, elemental mapping of carbon (C), nitrogen (N), and iron (Fe) were performed using EDS mapping. Distinct signals for all three elements were detected in both POPs, showing a uniform distribution across the examined areas without any noticeable aggregation, localized enrichment, or elemental depletion. These results confirm that the functional units, such as triazine and ferrocene, were successfully and homogeneously incorporated into the polymer backbone during the synthesis process. Transmission electron microscopy (TEM) combined with energy-dispersive X-ray spectroscopy (EDS) mapping was performed to examine the elemental distribution and structural uniformity of FC-TPT-POP and FC-TPT-Ph-POP [Figs. S5 and S6]. The TEM images reveal an irregular, aggregated morphology. The EDS elemental mapping clearly confirms the presence and spatial

distribution of carbon (C), nitrogen (N), and iron (Fe). Both SEM and TEM analysis confirm the successful incorporation and uniform distribution of carbon, nitrogen, and iron within the FC-TPT-POP and FC-TPT-Ph-POP. The observed structural uniformity highlights the effectiveness of the POPs design and element integration strategy, providing a strong foundation for its stability and performance in gas adsorption and catalytic applications.

3.2. *Comparative CO_2 capture efficiency of FC-TPT-POP and FC-TPT-Ph-POP*

The high surface area and heterogeneous pore size of FC-TPT-POP and FC-TPT-Ph-POP, combined with the presence of triazine units, make it highly promising for CO_2 capture. The triazine moieties introduce abundant nitrogen sites that can act as Lewis basic centers, enhancing the interaction with acidic CO_2 molecules. This synergistic combination of structural features ensures efficient adsorption capacity and selectivity toward CO_2. To investigate the gas adsorption and selectivity, the gas adsorption isotherms of CO_2 and N_2 were obtained at 273 and 298 K [Fig. 3]. The FC-TPT-POP and FC-TPT-Ph-POP demonstrated CO_2 capture of 3.34 and 2.52 mmol $g^{-1,}$ respectively, at 273 K. These values were reduced to 1.44 and 1.49 mmol $g^{-1,}$ respectively, at 298 K [Figs. 3**(a) and** 3**(b)**]. In contrast, the N_2 uptake was minimal, indicating that both POPs possess excellent CO_2 selectivity. The FC-TPT-POP and FC-TPT-Ph-POP displayed reduced N_2 uptake of 0.065 and 0.070 mmol g^{-1} at 298 K, while 0.149 and 0.115 mmol g^{-1} at 273 K, respectively [Figs. 3**(a) and** 3**(b)**]. The excellent CO_2 capture performance of both POPs is attributed to their high porosity, the nitrogen-rich s-triazine units (Lewis basic nitrogen sites), and Fe centers, which can enhance interactions with polar CO_2 molecules and contribute to greater adsorption capacity [68]. Moreover, the FC-TPT-POP demonstrates superior CO_2 adsorption performance than FC-TPT-Ph-POP due to its high surface and uniform microporosity, which is more favorable for CO_2 capture. In FC-TPT-Ph-POP, the additional biphenyl groups introduce greater steric hindrance and flexibility to the POP framework, resulting in a more disordered pore structure with broader pore size distribution and reduced packing density, which may weaken host-guest interactions and limit the effective adsorption of CO_2 as compared to FC-TPT-POP. To develop a clearer understanding of the interaction strength between the POPs and CO_2 molecules, the isosteric heat of adsorption (Q_{st}) was calculated as a function of CO_2 uptake using adsorption isotherms measured at different temperatures [Fig. 3**(c)**]. The FC-TPT-POP exhibits higher Q_{st} values across the entire CO_2 uptake range compared to FC-TPT-Ph-POP, indicating a stronger binding affinity toward CO_2. The

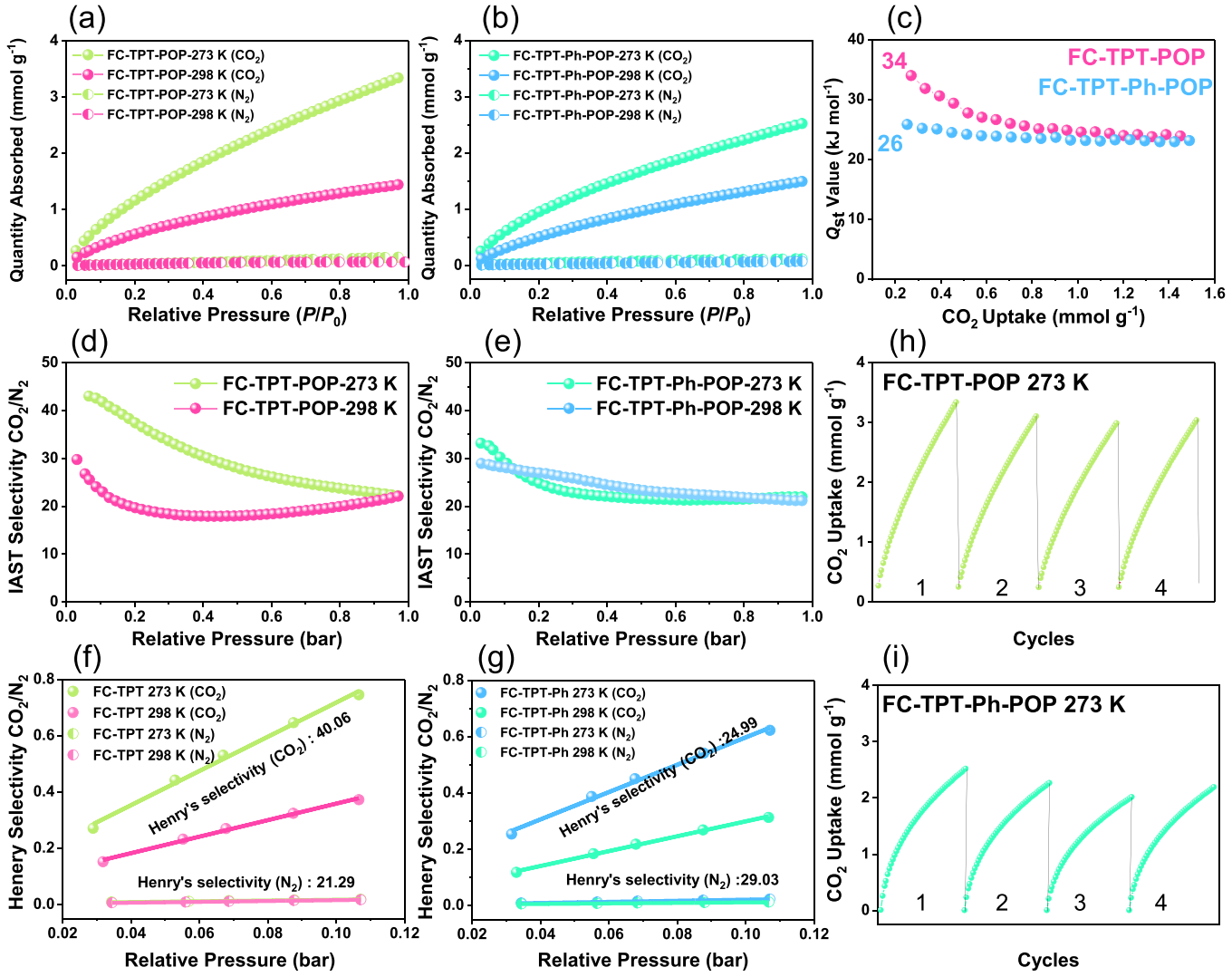

Fig. 3. (a, b) CO_2 and N_2 adsorption isotherms (uptake profiles); (c) isosteric heat of adsorption (Q_{st}) for CO_2; (d, e) CO_2/N_2 selectivity calculated by IAST; (f, g) CO_2/N_2 selectivity at low pressure (0.11 bar) estimated using Henry's law and (h, i) cyclic CO_2 adsorption stability and reusability tests for (h) FC-TPT-POP and (i) FC-TPT-Ph-POP, respectively.

Q_{st} corresponding to FC-TPT-POP begins at approximately 25 kJ mol^{-1} and gradually increases to ~32 kJ mol^{-1} with increasing uptake [Table S2]. This increasing trend indicates that CO_2 molecules first occupy adsorption sites with moderate binding energies and subsequently interact with higher energy sites, possibly because of cooperative adsorption behavior or gradual pore saturation. The enhanced binding affinity observed in FC-TPT-POP can be attributed to its higher surface area, microporosity, and nitrogen content, which facilitate stronger Lewis acid/base and π–π interactions with CO_2 molecules. However, FC-TPT-Ph-POP displays a relatively stable Q_{st} profile, ranging from 22 to 26 kJ mol^{-1}, indicating a more uniform but weaker physisorption process. This reduced interaction strength may be due to the presence of biphenyl moieties, which introduce steric hindrance and disrupt optimal CO_2 interactions. Both POPs exhibit the Q_{st} values within the range of 20–40 kJ mol^{-1}, suggesting that physical adsorption is more dominant in CO_2 capture. To further assess the gas separation performance of the POPs, the CO_2/N_2 selectivity was calculated at 273 K and 298 K using Ideal Adsorbed Solution Theory (IAST) [Figs. 3**(d) and** 3**(e)**]. Both POPs exhibited relatively high selectivity in the low-pressure region ($P/P_0 < 0.1$), which can be attributed to the higher polarity and quadrupole moment of CO_2 molecules. These properties promote stronger interactions with the nitrogen-containing active sites within the POP frameworks. The FC-TPT-POP displays significantly higher CO_2/N_2 selectivity than FC-TPT-Ph-POP at both temperatures, particularly at 273 K in the low-pressure region, where the selectivity reaches up to 40 [Table S2]. This indicates a stronger affinity of FC-TPT-POP toward CO_2 and a more effective exclusion of N_2 molecules. Moreover, FC-TPT-Ph-POP shows lower overall selectivity, with an unusual trend where its selectivity at 273 K is even lower than at 298 K. This inverse behavior may result from steric hindrance introduced by biphenyl moieties, which could impede gas diffusion or hinder access to adsorption sites. The elevated CO_2/N_2 selectivity observed for both POPs indicates a preferential interaction with CO_2 over N_2 under the tested conditions [69]. The CO_2/N_2 selectivity was also evaluated using Henry's law constants, derived from the early slopes of gas adsorption curves at low pressures (up to 0.11 bar) at 273 K and 298 K [Figs. 3**(f) and** 3**(g)**] [69]. Results showed that the FC-TPT-POP exhibited significantly enhanced selectivity for CO_2 over N_2 compared to the FC-TPT-Ph-POP. To assess the cyclic stability of the POPs for practical CO_2 capture applications, a three-cycle CO_2 adsorption/desorption test was performed at a constant temperature of 273 K [Figs. 3**(h) and** 3**(i)**]. The FC-TPT-POP exhibits highly stable CO_2 adsorption across all three cycles, with negligible loss in its maximum uptake capacity [Fig. 3**(f)**]. This behavior reflects excellent regenerability and structural integrity. The results align well with the Q_{st} analysis, indicating that the CO_2 adsorption in FC-TPT-POP is predominantly governed by reversible physisorption, supported by stable chemisorption interactions.

This dual adsorption mechanism facilitates efficient multi-cycle stability. In comparison, FC-TPT-Ph-POP displays a gradual decrease in CO_2 uptake with each cycle [Fig. 3**(i)**]. This suggests possible structural relaxation, partial pore blockage, or a loss of active sites during the regeneration process. Both POPs exhibit good cyclic stability; however, FC-TPT-POP demonstrates higher CO_2 uptake and superior reusability, underscoring its promise and reliability for long-term CO_2 capture applications. Fig. S7 shows the HOMO–LUMO isosurface maps of FC-TPT-POP and FC-TPT-Ph-POP. The HOMO of both molecules is primarily composed of the *d*-orbitals of Fe. LUMO is delocalized across the triazine and benzene rings, as well as the imine group linkage. The additional phenyl group in FC-TPT-Ph-POP further stabilizes the LUMO energy, shifting it from –1.85 to –1.89 eV, and reduces the HOMO–LUMO bandgap by 0.11 eV. Fig. S8 presents the molecular electrostatic potential (MESP) maps of FC-TPT-POP and FC-TPT-Ph-POP. This analysis quantitatively identifies the electrophilic and nucleophilic regions of each molecule, highlighting their most reactive sites. Areas of high electron density are shown in red, while regions of low electron density appear in blue. In both FC-TPT-POP and FC-TPT-Ph-POP, the most nucleophilic site corresponds to the lone pairs on the nitrogen atoms of the imine groups, exhibiting a negative electrostatic potential (ESP) of −30 kcal mol^{-1}. The nitrogen atoms within the triazine rings display slightly less negative ESP values of −21 kcal mol^{-1}. Conversely, the highest positive potential, around + 19 kcal mol^{-1}, is observed near the terminal hydrogen atoms of the cyclopentadienyl rings. Density functional theory (DFT) is one of the most widely used methods for investigating gas adsorption on POPs surfaces. In this study, DFT calculations were employed to determine the adsorption energies and geometries of CO_2 molecules on both FC-TPT-POP and FC-TPT-Ph-POP. Multiple possible adsorption sites were examined. The adsorption energies of CO_2 were calculated to be −5.75 kcal mol^{-1} on the imine group, −6.51 kcal mol^{-1} on the triazine ring, and −6.61 kcal mol^{-1} near the ferrocene moiety. These results indicate that the most favorable adsorption site is near the ferrocene moiety, which exhibits the most negative adsorption energy. However, the small difference in energy between the triazine and ferrocene sites suggests that adsorption is likely to occur on both, reflecting a dynamic equilibrium. Fig. S9 illustrates the optimized structure of the most stable complex formed between CO_2 and FC-TPT-POP, along with the reduced density gradient (RDG) plot depicting the nature of intermolecular interactions. RDG analysis is a powerful approach for visualizing noncovalent interactions. The CO_2 molecule exhibits π–π interactions with the phenyl group, while its negatively charged oxygen atoms engage in ionic interactions with the hydrogen atoms of both the ferrocene moiety and the imine group. The interaction with the ferrocene hydrogen is stronger, as evidenced by its shorter bond length. These findings are consistent with MESP results shown in Fig. S8, which revealed that the hydrogens on the ferrocene moiety possess the highest positive electrostatic potential within the molecule. A similar adsorption behavior was observed for FC-TPT-Ph-POP. The most favorable site for CO_2 adsorption was located near the ferrocene moiety, followed by the triazine ring, with corresponding adsorption energies of −6.90 and −6.57 kcal mol^{-1}. The electronegativity (χ) and chemical hardness (η) of the three species were calculated based on their HOMO and LUMO energies. The χ values for FC-TPT-POP, FC-TPT-Ph-POP, and CO_2 were 3.68, 3.65, and 4.63 eV, respectively. Since both polymers exhibit lower electronegativity than CO_2, electron transfer occurs from the polymer to the CO_2 molecule upon adsorption. The fraction of electron transfer (Δ*N*) from the polymer to CO_2 can be estimated using Pearson's theory as follows [70]: $\Delta N = (\chi_{CO_2} - \chi_{Polymer})/2(\eta_{CO_2} + \eta_{POP})$, and Δ*N* for both POPs was 0.07.

3.3. Catalytic conversion performance of CO_2 into cyclic carbonates using FC-TPT-Ph-POP and FC-TPT-POP

The synthesis of cyclic carbonates from CO_2 and epoxides represents an efficient and environmentally friendly strategy for CO_2 utilization. This transformation not only offers a sustainable approach to mitigate greenhouse gas emissions but also produces high-value cyclic carbonates, which are widely used as green solvents, electrolytes in batteries [26,71,72]. Motivated by the presence of Lewis acidic ferrocene units and nitrogen-rich triazine moieties in our synthesized POP, we investigated its catalytic potential for the cycloaddition of CO_2 with epoxides by employing PPNCl as a catalyst. The experiments were conducted using a stainless-steel autoclave at a constant CO_2 pressure of 400 psi and a temperature of 120 °C [Fig. 4**(a)**]. Firstly, control experiments were carried out using PO as the model monomer, FC-TPT-POP, and PPNCl as the catalyst [Fig. 4**(b)**]. When FC-TPT-POP was used alone as a catalyst, the conversion of PO to cyclic carbonate was only 1.2 %, indicating limited catalytic activity and suggesting that the POP catalyst alone is insufficient to effectively initiate the ring-opening of the epoxide [Figs. 4**(b) and** 4**(c)**]. In contrast, the use of PPNCl without the POP catalyst resulted in a significantly higher conversion of 67.1 %, highlighting the crucial role of the catalyst in activating the epoxide. No product formation was observed in the absence of both catalysts, confirming that thermal background reactions are negligible under these

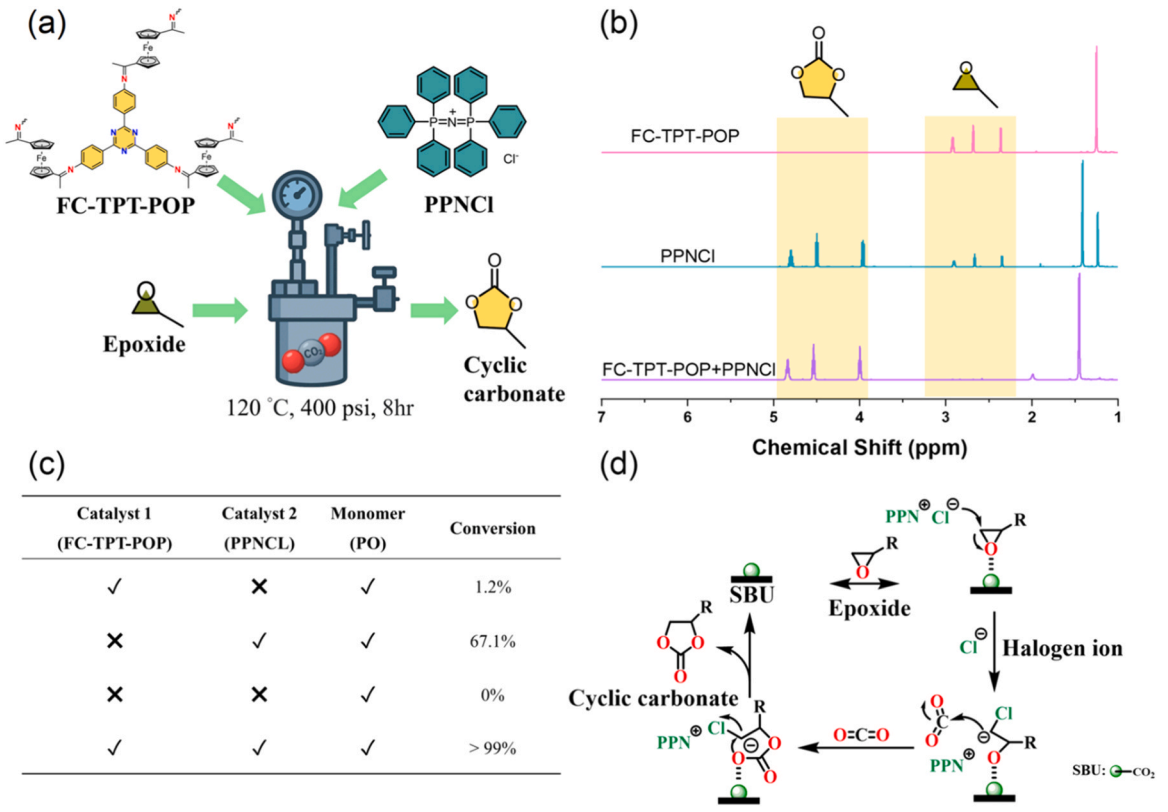

Catalyst 1 (FC-TPT-POP)	Catalyst 2 (PPNCL)	Monomer (PO)	Conversion
✓	✕	✓	1.2%
✕	✓	✓	67.1%
✕	✕	✓	0%
✓	✓	✓	> 99%

Fig. 4. (a) Schematic representation of reaction conditions for CO_2 utilization, (b) ^1H NMR of initial catalyst testing, (c) conversion rate, and (d) possible mechanism of epoxide conversion using PPNCl catalyst.

conditions. Remarkably, when FC-TPT-POP was combined with PPNCl, the conversion of PO exceeded 99 %, clearly demonstrating a strong synergistic catalytic effect between the two catalysts [Figs. 4**(b) and** 4 **(c)**]. The proposed reaction mechanism is illustrated in [Fig. 4**(d)**]. Initially, assisted by the catalyst PPNCl, the chloride ion (Cl^-) performs a nucleophilic attack on the epoxide ring, promoting its ring opening to form a reactive alkoxide intermediate. During this step, the nitrogen-rich triazine units within the FC-TPT-POP structure act as Lewis bases to stabilize the developing positive charge, while additional interactions such as hydrogen bonding and π–π stacking enhance the local concentration and activation of CO_2 molecules.

Subsequently, the activated alkoxide intermediate reacts with CO_2, which is efficiently concentrated and stabilized by the PPNCl catalyst. This interaction promotes cyclization, resulting in the formation of a five-membered cyclic carbonate [Fig. 4**(d)**]. Figs. S10 and S11 propose a plausible catalytic pathway for the CO_2/epoxide cycloaddition reaction promoted by the dual-catalyst system of FC-TPT-POP or FC-TPT-Ph-POP and PPNCl. In this mechanism, Fe^{2+} centers within the CMP framework function as Lewis acid sites, coordinating to the epoxide oxygen and inducing polarization of the C–O bonds, thereby facilitating substrate activation. Subsequently, the chloride anion (Cl^-) supplied by PPNCl performs a nucleophilic attack on the β-carbon of the activated epoxide, leading to ring-opening and formation of an oxyanion intermediate. The electron-rich triazine rings further stabilize and concentrate CO_2 molecules in proximity via non-covalent lone-pair···π interactions, increasing local CO_2 availability at the reaction interface. The nucleophilic oxygen of the intermediate then attacks CO_2, followed by intramolecular cyclization, ultimately yielding cyclic carbonate products [73,74]. The overall reaction benefits from the porous nature of the FC-TPT-POP, which facilitates efficient mass transport. At the same time, nitrogen sites and iron centers further contribute to directional adsorption and catalytic stabilization, ultimately enabling high conversion. These findings highlight the cooperative nature of the catalytic system and confirm the potential of FC-TPT-POP as a heterogeneous catalyst for CO_2 fixation into cyclic carbonates when paired with an appropriate catalyst. To further investigate the effect of structural variation on catalytic performance, we evaluated another POP, FC-TPT-Ph-POP, under identical reaction conditions and PO monomer. Compared to FC-TPT-POP, FC-TPT-Ph-POP exhibited lower catalytic efficiency, achieving only 85 % PO conversion [Fig. S12]. This result suggests that the structural features of FC-TPT-POP, such as enhanced electron density or greater active site accessibility, may contribute to its superior catalytic activity. Given its superior catalytic performance, FC-TPT-POP was selected for further investigation. Subsequent studies focused on evaluating its catalytic efficiency across a range of epoxide substrates to assess its versatility and substrate scope in the cycloaddition reaction with CO_2. Fig. S13 shows CO_2 adsorbed on the triazine ring of the FC-TPT-POP and FC-TPT-Ph-POP. The green color shows van der Waals interactions between the two molecules. The amount of charge transfer from the triazine ring FC-TPT-POP and FC-TPT-Ph-POP to the CO_2 was 0.07 electron, according to the Pearson theory. The DFT results indicate that triazine N atoms not only act as CO_2 binding sites but also participate electronically by donating electron density to adjacent catalytic centers, facilitating charge redistribution in the cycle. The charge transfer suggests that triazine N enables electron migration, lowering the activation barrier of the ring-opening/CO_2-insertion step proposed in Figs. S10 and S11. Explicitly linking this electron-transfer behavior to catalyst regeneration would further solidify their synergistic mechanism.

To optimize the catalytic performance of FC-TPT-POP in the cycloaddition reaction between CO_2 and PO, we further assessed how changes in reaction temperature and time affect the process's catalytic efficiency [Fig. 5]. The temperature-dependent experiments were conducted under a fixed reaction time of 8 h [Fig. 5**(a)**] . The results revealed a strong temperature dependence; the conversion was only 11.2 % at 80 °C, increased to 30.7 % at 100 °C, and reached nearly complete conversion (99.5 %) at 120 °C, indicating that elevated temperatures significantly

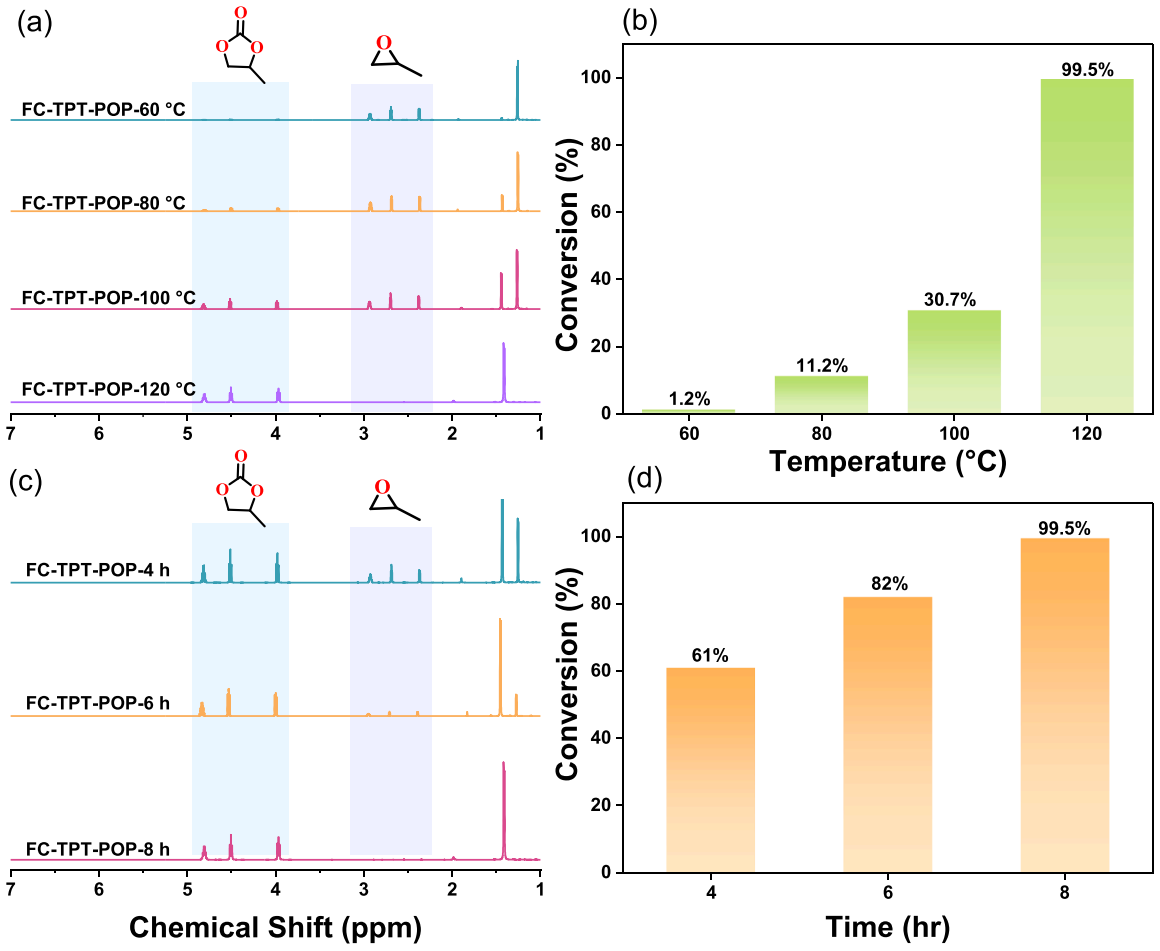

Fig. 5. Conversion of PO to cyclic carbonate using FC-TPT-POP as catalyst (a) ^{1}H NMR profiles at different temperatures, (b) conversion to cyclic carbonates percentage at different temperatures, (c) ^{1}H NMR profiles at different times, and (d) conversion to cyclic carbonates percentage at different times.

enhance both reaction rate and efficiency [Fig. 5**(b)**]. Furthermore, under a constant temperature of 120 °C, the effect of reaction time was examined [Fig. 5**(c)**]. The conversion increased from 61 % to 82 % in 6 h, and finally to 99.5 % in 8 h [Fig. 5**(d)**]. These findings confirm that FC-TPT-POP possesses excellent catalytic activity and stability under high-temperature conditions. The optimal conditions were determined to be 120 °C for 8 h, under which high conversion efficiency can be achieved. This demonstrates the potential of FC-TPT-POP for efficient CO_2 capture and the synthesis of value-added cyclic carbonates. To further evaluate the substrate scope of FC-TPT-POP, a series of different epoxide monomers, including PO, PGE, *t*-BGE, CHO, and EHGE, was used [Fig. 6]. All reactions were conducted under identical conditions, 120 °C and 400 psi CO_2 pressure, and the conversion rates were compared at 8 and 24 h. This allowed us to investigate the influence of epoxide structure on reaction kinetics and overall efficiency in the cycloaddition of CO_2 to form cyclic carbonates. The PO exhibited the highest reactivity, achieving a near-complete conversion of 99.5 % within just 8 h [Fig. 6**(a)**]. This can be attributed to its simple molecular structure, high ring strain, and well-exposed epoxide group, which favor efficient interaction with CO_2. The PGE contains a bulky aromatic ring; its flexible ether side chain helps alleviate steric hindrance by increasing the accessible space around the reactive site. This structural feature facilitates CO_2 diffusion and insertion, resulting in a high conversion rate of 95–96 % within 8 h [Fig. 6**(b)** and Table S3]. The *t*-BGE bears a large *tert*-butyl substituent that introduces significant steric hindrance. Despite also possessing an ether linkage, its conversion rate at 8 h was only 71.2 %, requiring 24 h to reach 99 % [Fig. 6**(c)**] [Table S3]. This indicates that substantial steric bulk can slow down the reaction kinetics, necessitating longer reaction times. The EHGE, though structurally larger, contains a flexible and branched alkyl chain with a high degree of free volume. This enhances CO_2 diffusion and access to the catalytic sites, resulting in a conversion of 85.8 % at 8 h and 100 % at 24 h [Fig. 6**(d)**] [Table S3].

These results suggest that, in certain cases, molecular flexibility and free volume can compensate for steric limitations. Cyclohexene oxide (CHO), with its six-membered ring structure, exhibited the lowest reactivity among all tested monomers. Its low ring strain and poor accessibility of the epoxide group significantly hinder its activation by the catalyst, leading to conversion rates of only 39 % and 43 % at 8 and 24 h, respectively [Fig. 6**(d)** and Table S3]. The conversion efficiency of different epoxides is strongly influenced by their molecular structure, including steric hindrance, chain flexibility, free volume, and ring strain. These findings not only highlight the broad applicability of the POP catalyst but also offer valuable insights into structure–activity relationships in CO_2 conversion reactions. After evaluating various epoxy monomers for their conversion into cyclic carbonates, PO was selected for recyclability studies due to its superior conversion efficiency. A five-cycle reuse test was conducted to assess the catalytic stability and reusability of the materials over multiple reactions [Fig. 7]. The FTIR spectra revealed a distinct C═O stretching vibration around 1800 cm^{-1} in the reaction products, confirming the successful formation of cyclic carbonates after five cycles [Figs. 7**(a) and** 7**(d)**]. The ^{1}H NMR spectra further validated the FTIR results, confirming the effective conversion of PO into cyclic carbonates upon recycling [Figs. 7**(b) and** 7**(e)**]. The FC-TPT-POP catalyst demonstrated excellent catalytic performance and cycling stability, achieving conversion rates of 99.5 %, 98 %, 95 %,

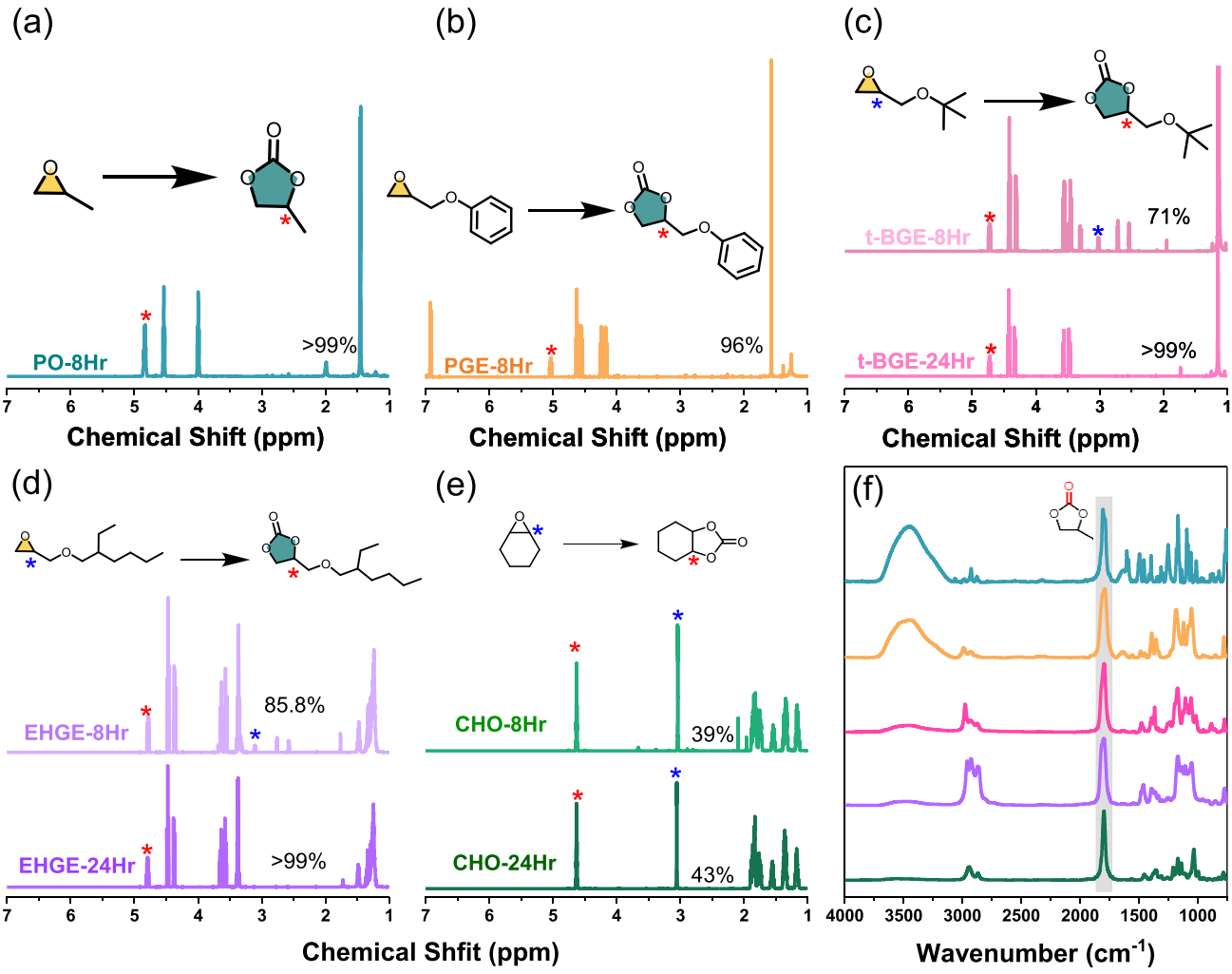

Fig. 6. ^{1}H NMR profiles for the conversion of different epoxides to cyclic carbonates using FC-TPT-POP as a catalyst. (a) PO, (b) PGE, (c) *t*-BGE, (d) EHGE, (e) CHO, at different times, (f) FTIR of cyclic carbonates using different epoxides.

92 %, and 88 % over five consecutive cycles [Fig. 7**(c)**]. In comparison, FC-TPT-Ph-POP also exhibited catalytic activity but with lower and progressively declining conversion rates of 85 %, 82 %, 78 %, 74 %, and 70 % [Fig. 7**(f)**]. Importantly, both catalysts could be reused directly without any regeneration, highlighting their promising recyclability and practical applicability as heterogeneous catalytic systems. As summarized in Table S4, both FC-TPT-POP and FC-TPT-Ph-POP exhibit outstanding catalytic performance for the cycloaddition reaction of CO_2 with propylene oxide (PO) to form cyclic carbonate under solvent-free conditions. Compared with previously reported POPs and metal–organic frameworks (MOFs).

4. Conclusions

In this study, two POPs, designated FC-TPT-POP and FC-TPT-Ph-POP, were successfully synthesized via a Schiff base reaction using triazine- and ferrocene-based monomers. Their performance in CO_2 capture and catalytic conversion was systematically investigated. Nitrogen sorption analysis revealed that FC-TPT-POP exhibited a higher BET surface area (797 m^2/g) and a uniform pore size distribution, which enabled superior CO_2 uptake and improved separation selectivity. Catalytic tests with five different epoxides (PO, PGE, *t*-BGE, CHO, and EHGE) demonstrated that FC-TPT-POP achieved the highest catalytic performance, reaching 99.5 % conversion of PO at 120 °C and 400 psi CO_2 within 8 h. The reactivity of the epoxides was strongly influenced by their molecular structures, including ring strain, steric hindrance, free volume, and chain flexibility. Both POP catalysts displayed excellent reusability as heterogeneous systems. FC-TPT-POP maintained conversion rates above 98 % across three consecutive cycles without notable loss of activity or structural integrity. This underscores the practical advantages of these POPs, particularly in terms of recyclability and ease of operation, when compared to conventional homogeneous catalysts. Overall, this study demonstrates the rational design and functional integration of triazine–ferrocene-based POPs for efficient CO_2 capture and catalytic conversion. The synergy of high nitrogen content, tunable porosity, and robust heterogeneous stability renders these materials highly promising for sustainable carbon utilization and environmentally friendly catalytic applications.

CRediT authorship contribution statement

Wei-Chun Huang: Investigation, Data curation. **Mohsin Ejaz:** Writing – review & editing, Writing – original draft, Formal analysis, Data curation. **Yang-Chin Kao:** Data curation. **Yen-Min Lo:** Methodology, Investigation. **Ahmed A. K. Mohammed:** Software. **Yen-Ling Kuan:** Data curation. **Shiao-Wei Kuo:** Supervision, Resources, Project administration. **Mohamed Gamal Mohamed:** Writing – review & editing, Writing – original draft, Supervision, Methodology,

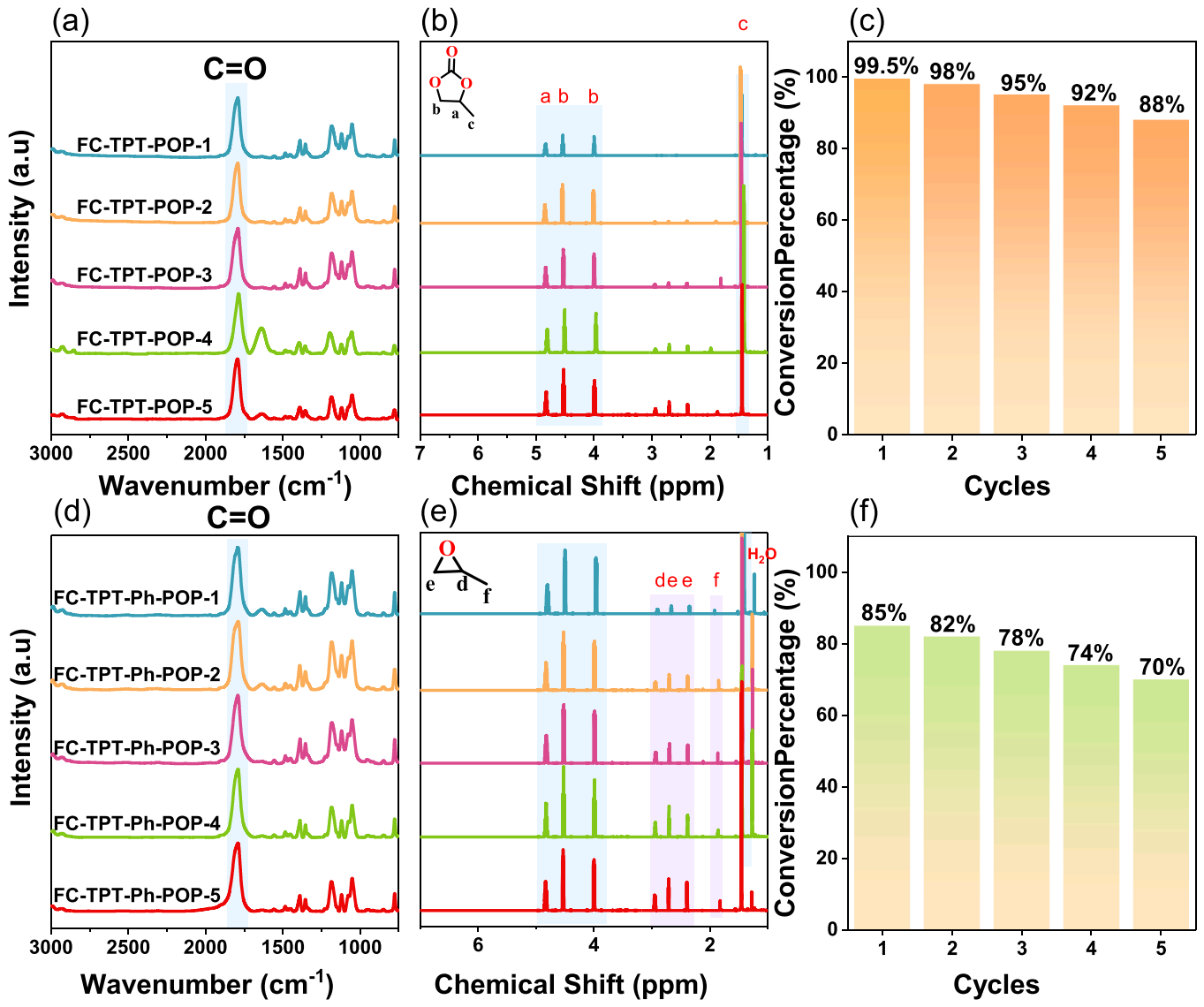

Fig. 7. Cyclic performance tests for the conversion of PO to cyclic carbonates using (a) FTIR, (b) ^{1}H NMR, and (c) conversion percentage for FC-TPT-POP, and (d) FTIR, (e) ^{1}H NMR, and (f) conversion percentage for FC-TPT-Ph-POP.

Investigation, Formal analysis, Data curation, Conceptualization.

Declaration of Competing Interest

The authors declare that they have no known competing financial interests or personal relationships that could have appeared to influence the work reported in this paper.

Acknowledgments

This study was supported financially by the National Science and Technology Council, Taiwan, under Contracts NSTC 114-2223-E-110-001- and 113-2221-E-110-012-MY3. The authors thank the staff at National Sun Yat-sen University for their assistance with the TEM (ID: EM022600) experiments.

Appendix A. Supporting information

Supplementary data associated with this article can be found in the online version at doi:10.1016/j.jcou.2026.103356.

Data availability

Data will be made available on request.

References

[1] I.A.R. Kiribou, T. Neya, B. Nana, K. Ogunjobi, T. Daho, Y.W. Gounkaou, F. M. Muema, D.W. Sintayehu, Road transport and urban mobility greenhouse gas emissions factor for air pollution modeling in Burkina Faso, J. Urban Mobil. 7 (2025) 100106, https://doi.org/10.1016/j.urbmob.2025.100106.

[2] T. Choudhury, U.N. Kayani, A. Gul, S.A. Haider, S. Ahmad, Carbon emissions, environmental distortions, and impact on growth, Energy Econ. 126 (2023) 107040, https://doi.org/10.1016/j.eneco.2023.107040.

[3] W.E. Parker, M.K. Brown, R. Linares, Greenhouse gases reduce the satellite carrying capacity of low Earth orbit, Nat. Sustain. 8 (2025) 363–372, https://doi.org/10.1038/s41893-025-01512-0.

[4] H. Li, J. Qiu, K. Zhang, B. Zheng, Monitoring fossil fuel CO_2 emissions from co-emitted NO_2 observed from space: progress, challenges, and future perspectives, Front. Environ. Sci. Eng. 19 (2024) 2, https://doi.org/10.1007/s11783-025-1922-x.

[5] A. Yakymchuk, M.A. Rataj, Economic analysis of fossil CO_2 emissions: a European perspective on sustainable development, Energies 18 (2025) 2106, https://doi.org/10.3390/en18082106.

[6] Y. Shi, W. Su, Y. Xing, Y. Cui, X. Liu, W. Guo, Z. Che, Research progress and future prospects of chemical utilization of CO_2, Chem. Eng. J. 510 (2025) 161579, https://doi.org/10.1016/j.cej.2025.161579.

[7] E. Sivasurya, R. Atchudan, M.G. Mohamed, A. Thangamani, S. Rajendran, A. Jalil, P.K. Kalambate, D. Manoj, S.W. Kuo, Electrocatalytic conversion of CO_2 into selective carbonaceous fuels using metal-organic frameworks: an overview of recent progress and perspectives, Mater. Today Chem. 44 (2025) 102538, https://doi.org/10.1016/j.mtchem.2025.102538.

[8] D. Shindell, J. Rogelj, Preserving carbon dioxide removal to serve critical needs, Nat. Clim. Change 15 (2025) 452–457, https://doi.org/10.1038/s41558-025-02251-y.

[9] S. Afrane, J.D. Ampah, H. Adun, J.L. Chen, H. Zou, G. Mao, P. Yang, Targeted carbon dioxide removal measures are essential for the cost and energy transformation of the electricity sector by 2050, Commun. Earth Environ. 6 (2025) 227, https://doi.org/10.1038/s43247-025-02190-8.

[10] H.-J. Yoon, T.A. Atsbha, T. Yoon, D. Shin, J. An, M. Zarei, A. Cherif, S. Suh, C.-J. Lee, Sustainable and feasible carbon capture and utilization pathways towards net-zero, Renew. Sustain. Energy Rev. 211 (2025) 115331, https://doi.org/10.1016/j.rser.2025.115331.

[11] J. Sadhukhan, O.J. Fisher, B. Cummings, J. Xuan, Novel comprehensive life cycle assessment (LCA) of sustainable flue gas carbon capture and utilization (CCU) for surfactant and fuel via Fischer-Tropsch synthesis, J. CO_2 Util. 92 (2025) 103013, https://doi.org/10.1016/j.jcou.2024.103013.

[12] M.P. Lanting, J.A. Voogt, K.P.H. Meesters, D.S. van Es, M. Bekker, M.E. Bruins, Prospective techno-economic assessment of carbon capture & utilization and biobased processes for methanol and ethanol production, Sustain. Energy Fuels 9 (2025) 4660–4673, https://doi.org/10.1039/D5SE00435G.

[13] N. Wang, J. Zhou, J. Ren, Recent advances in CO_2 capture and utilization: from the perspective of process integration and optimization, Renew. Sustain. Energy Rev. 216 (2025) 115688, https://doi.org/10.1016/j.rser.2025.115688.

[14] O. Awogbemi, D.A. Desai, Novel technologies for CO_2 conversion to renewable fuels, chemicals, and value-added products, Discov. Nano 20 (2025) 29, https://doi.org/10.1186/s11671-025-04214-w.

[15] J. Ye, N. Dimitratos, L.M. Rossi, N. Thonemann, A.M. Beale, R. Wojcieszak, Hydrogenation of CO_2 for sustainable fuel and chemical production, Science 387 (2025) eadn9388, https://doi.org/10.1126/science.adn9388.

[16] M. Ejaz, M.G. Mohamed, S.-W. Kuo, Solid state chemical transformation provides a fully benzoxazine-linked porous organic polymer displaying enhanced CO_2 capture and supercapacitor performance, Polym. Chem. 14 (2023) 2494–2509, https://doi.org/10.1039/D3PY00158J.

[17] M. Pera-Titus, Porous inorganic membranes for CO_2 capture: present and prospects, Chem. Rev. 114 (2014) 1413–1492, https://doi.org/10.1021/cr400237k.

[18] M. Ejaz, M.G. Mohamed, Y.-T. Chen, K. Zhang, S.-W. Kuo, Porous carbon materials augmented with heteroatoms derived from hyperbranched biobased benzoxazine resins for enhanced CO_2 adsorption and exceptional supercapacitor performance, J. Energy Storage 78 (2024) 110166, https://doi.org/10.1016/j.est.2023.110166.

[19] G. Xu, L. Li, Y. Yang, L. Tian, T. Liu, K. Zhang, A novel CO_2 cryogenic liquefaction and separation system, Energy 42 (2012) 522–529, https://doi.org/10.1016/j.energy.2012.02.048.

[20] L. Guo, R. Dou, Y. Wu, R. Zhang, L. Wang, Y. Wang, Z. Gong, J. Chen, X. Wu, From lignin waste to efficient catalyst: illuminating the impact of lignin structure on catalytic activity of cycloaddition reaction, ACS Sustain. Chem. Eng. 7 (2019) 16585–16594, https://doi.org/10.1021/acssuschemeng.9b03909.

[21] M. Liu, C. Ma, Q. Wang, R. Li, S. Yu, H. Chen, F. Liu, Capture and in-situ conversion of low-concentration CO_2 over robust poly(ionic liquid)@porous carbon nanocomposites under green, co-catalyst- and solvent-free conditions, Chem. Eng. J. 499 (2024) 155635, https://doi.org/10.1016/j.cej.2024.157099.

[22] W. Jaroonwatana, T. Theerathanagorn, M. Theerasilp, S.D. Gobbo, D. Yiamsawas, V.D. Elia, D. Crespy, Nanoparticles of aromatic biopolymers catalyze CO_2 cycloaddition to epoxides under atmospheric conditions, Sustain. Energy Fuels 5 (2021) 5431–5444, https://doi.org/10.1039/D1SE01305J.

[23] W. Natongchai, D. Crespy, V. D'Elia, CO_2 fixation: cycloaddition of CO_2 to epoxides using practical metal-free recyclable catalysts, Chem. Commun. 61 (2025) 419–440, https://doi.org/10.1039/D4CC05291A.

[24] X. Xu, Y. Sui, W. Chen, L. Chai, X. Li, W. Huang, G. Zhou, Y. Li, H. Zhong, Imidazolium-based ionic polymers containing electrostatic and triple hydrogen bond for efficient conversion of CO_2 into cyclic carbonates, ChemCatChem 17 (2025) e202402130, https://doi.org/10.1002/cctc.202402130.

[25] P.P. Pescarmona, Cyclic carbonates synthesised from CO_2: applications, challenges and recent research trends, Curr. Opin. Green Sustain. Chem. 29 (2021) 100457, https://doi.org/10.1016/j.cogsc.2021.100457.

[26] P. Rollin, L.K. Soares, A.M. Barcellos, D.R. Araujo, E.J. Lenardão, R.G. Jacob, G. Perin, Five-membered cyclic carbonates: versatility for applications in organic synthesis, Pharm. Mater. Sci. Appl. Sci. 11 (2021) 5024, https://doi.org/10.3390/app11115024.

[27] S. Fukuoka, M. Kawamura, K. Komiya, M. Tojo, H. Hachiya, K. Hasegawa, M. Aminaka, H. Okamoto, I. Fukawad, S. Konno, A novel non-phosgene polycarbonate production process using by-product CO_2 as starting material, Green Chem. 5 (2003) 497–507, https://doi.org/10.1039/B304963A.

[28] T. Theerathanagorn, T. Kessaratikoon, H. Ur Rehman, V.D. Elia, D. Crespy, Polyhydroxyurethanes from biobased monomers and CO_2: a bridge between sustainable chemistry and CO_2 utilization, Chin. J. Chem. 42 (2024) 652–685, https://doi.org/10.1002/cjoc.202300531.

[29] L. Maisonneuve, O. Lamarzelle, E. Rix, E. Grau, H. Cramail, Isocyanate-free routes to polyurethanes and poly(hydroxy urethane)s, Chem. Rev. 115 (2015) 12407–12439, https://doi.org/10.1021/acs.chemrev.5b00355.

[30] M.G. Mohamed, B. Halder, P.N. Singh, A.A.K. Mohammed, P. Elumalai, S.-W. Kuo, Molecular engineering and synergistic redox-active hexaazatrinaphthalene and pyrene-based conjugated microporous polymers for superior faradaic supercapacitor energy storage, Chem. Eng. J. 520 (2025) 165892, https://doi.org/10.1016/j.cej.2025.165892.

[31] M. Ejaz, M.G. Mohamed, W.-C. Chang, S.-W. Kuo, Synthesis and design of hypercrosslinked porous organic frameworks containing tetraphenylpyrazine unit for high-performance supercapacitor, J. Polym. Sci. 62 (2024) 1629–1638, https://doi.org/10.1002/pol.20230174.

[32] Y.-C. Kao, K.-T. Yeh, M.G. Mohamed, H. Karim, W.-H. Su, S.-W. Kuo, Structural modulation via mesoporous silica templating in covalent organic frameworks: converting functional aspects for adsorption behavior, Sep. Purif. Technol. 375 (2025) 133827, https://doi.org/10.1016/j.seppur.2025.133827.

[33] M. Ejaz, M.G. Mohamed, M.G. Kotp, A.M. Elewa, S.-W. Kuo, Triphenylamine-linked triazine (D-A) units based hypercrosslinked porous polymer: rapid adsorption and enhanced photodegradation of organic dyes from water, Colloids Surf. A Physicochem. Eng. Asp. 722 (2025) 137239, https://doi.org/10.1016/j.colsurfa.2025.137239.

[34] M. Ejaz, M.G. Mohamed, S.-W. Kuo, Benzoxazine-linked polyhedral oligomeric silsesquioxane: 3D porous organic-inorganic polymer for improved CO_2 capture and supercapacitor performance, J. Taiwan Inst. Chem. Eng. (2025) 106098, https://doi.org/10.1016/j.jtice.2025.106098.

[35] M. Ejaz, M.G. Mohamed, W.-C. Huang, S.-W. Kuo, Pyrene-based covalent organic polymers with nano carbonaceous composites for efficient supercapacitive energy storage, J. Mater. Chem. A 11 (2023) 22868–22883, https://doi.org/10.1039/D3TA02741D.

[36] M. Ejaz, M.G. Mohamed, S.-W. Kuo, Fluorescent benzoxazine–perylene linked covalent organic polymer as a sensing probe for lead ions and 2,4,6-trinitrophenol, ACS Appl. Polym. Mater. 6 (2024) 9170–9179, https://doi.org/10.1021/acsapm.4c01514.

[37] M.G. Mohamed, I.M.A. Mekhemer, A.F.H. Selim, A. Katsamitros, D. Tasis, A. Basit, H.-H. Chou, S.-W. Kuo, Molecular engineering of donor–acceptor-type conjugated microporous polymers for dual effective photocatalytic production of hydrogen and hydrogen peroxide, Mater. Horiz. 12 (2025) 5917–5928, https://doi.org/10.1039/D5MH00735F.

[38] M. Mohamed Samy, I.M.A. Mekhemer, M.G. Mohamed, M. Hammad Elsayed, K.-H. Lin, Y.-K. Chen, T.-L. Wu, H.-H. Chou, S.-W. Kuo, Conjugated microporous polymers incorporating thiazolo[5,4-d]thiazole moieties for sunlight-driven hydrogen production from water, Chem. Eng. J. 446 (2022) 137158, https://doi.org/10.1016/j.cej.2022.137158.

[39] M.G. Mohamed, A.F.M. El-Mahdy, M.G. Kotp, S.-W. Kuo, Advances in porous organic polymers: syntheses, structures, and diverse applications, Mater. Adv. 3 (2022) 707–733, https://doi.org/10.1039/D1MA00771H.

[40] S. Kumar, R. Srivastava, J. Koh, Utilization of zeolites as CO_2 capturing agents: advances and future perspectives, J. CO_2 Util. 41 (2020) 101251, https://doi.org/10.1016/j.jcou.2020.101251.

[41] D.B. Rothschild, J. Chen, Z. Wan, S. Renneckar, I. Burgert, Y. Ding, Y. Lu, O. J. Rojas, Lignin-based porous carbon adsorbents for CO_2 capture, Chem. Soc. Rev. 54 (2025) 623–652, https://doi.org/10.1039/D4CS00923A.

[42] H. Demir, G.O. Aksu, H.C. Gulbalkan, S. Keskin, MOF membranes for CO_2 capture: past, present and future, Carbon Capture Sci. Technol. 2 (2022) 100026, https://doi.org/10.1016/j.ccst.2021.100026.

[43] M.G. Mohamed, B.-X. Su, S.-W. Kuo, Robust nitrogen-doped microporous carbon via crown ether-functionalized benzoxazine-linked porous organic polymers for enhanced CO_2 adsorption and supercapacitor applications, ACS Appl. Mater. Interfaces 16 (2024) 40858–40872, https://doi.org/10.1021/acsami.4c05645.

[44] S. Zeng, X. Zhang, L. Bai, X. Zhang, H. Wang, J. Wang, D. Bao, M. Li, X. Liu, S. Zhang, Ionic-liquid-based CO_2 capture systems: structure, interaction and process, Chem. Rev. 117 (2017) 9625–9673, https://doi.org/10.1021/acs.chemrev.7b00072.

[45] M. Wang, A. Lawal, P. Stephenson, J. Sidders, C. Ramshaw, Post-combustion CO_2 capture with chemical absorption: a state-of-the-art review, Chem. Eng. Res. Des. 89 (2011) 1609–1624, https://doi.org/10.1016/j.cherd.2010.11.005.

[46] H. Akaya, S. Lamnini, H. Sehaqui, J. Jacquemin, Amine-functionalized cellulose as promising materials for direct CO_2 capture: a review, ACS Appl. Mater. Interfaces 17 (2025) 16380–16395, https://doi.org/10.1021/acsami.4c20801.

[47] S. Wei, M.K. Albolkany, L. Zhao, B. Liu, Supramolecular chemistry for carbon dioxide capture, Coord. Chem. Rev. 535 (2025) 216655, https://doi.org/10.1016/j.ccr.2025.216655.

[48] Y. Zhang, S.N. Riduan, Functional porous organic polymers for heterogeneous catalysis, Chem. Soc. Rev. 41 (2012) 2083–2094, https://doi.org/10.1039/C1CS15227K.

[49] K.S. Song, P.W. Fritz, A. Coskun, Porous organic polymers for CO_2 capture, separation and conversion, Chem. Soc. Rev. 51 (2022) 9831–9852, https://doi.org/10.1039/D2CS00727D.

[50] S. Nagireddi, J.R. Agarwal, D. Vedapuri, Carbon dioxide capture, utilization, and sequestration: current status, challenges, and future prospects for global decarbonization, ACS Eng. Au 4 (2024) 22–48, https://doi.org/10.1021/acsengineeringau.3c00049.

[51] R. Ping, L. He, Q. Wang, F. Liu, H. Chen, S. Yu, K. Gao, M. Liu, Unveiling the incorporation of dual hydrogen-bond-donating squaramide moieties into covalent triazine frameworks for promoting low-concentration CO_2 fixation, Appl. Catal. B Environ. Energy 365 (2025) 124895, https://doi.org/10.1016/j.apcatb.2024.124895.

[52] H. Zhang, W. Zhang, F. Liu, Z.H. Luo, K. Gao, M. Liu, Unveiling the integrated function of metallo-/ionic-covalent organic polymers for boosting atmospheric CO_2 conversion, AIChE J. 70 (2024) e18488, https://doi.org/10.1002/aic.18488.

[53] T. Qu, X. Duan, Z. Ma, F. Liu, J. Ma, K. Gao, M. Liu, Experimental and theoretical investigation of phenylpyridine-based hypercrosslinked polymers for atmospheric CO_2 adsorption and fixation under solvent-/metal-free conditions, Chem. Eng. Sci. 297 (2024) 120298, https://doi.org/10.1016/j.ces.2024.120298.
[54] H. Wang, D. Jiang, D. Huang, G. Zeng, P. Xu, C. Lai, M. Chen, M. Cheng, C. Zhang, Z. Wang, Covalent triazine frameworks for carbon dioxide capture, J. Mater. Chem. A 7 (2019) 22848–22870, https://doi.org/10.1039/C9TA06847C.
[55] O. Buyukcakir, S.H. Je, S.N. Talapaneni, D. Kim, A. Coskun, Charged covalent triazine frameworks for CO_2 capture and conversion, ACS Appl. Mater. Interfaces 9 (2017) 7209–7216, https://doi.org/10.1021/acsami.6b16769.
[56] Y. Zhao, Y. Hu, Y. Ma, L. Ding, S. Zhang, Y. Fu, X. Wang, The enhanced adsorption towards CO_2 via ammonification and mechanism investigation for covalent triazine porous material based on density functional theory study, Appl. Surf. Sci. 685 (2025) 161963, https://doi.org/10.1016/j.apsusc.2024.161963.
[57] A. Straube, L. Useini, E. Hey-Hawkins, Multi-ferrocene-based ligands: from design to applications, Chem. Rev. 125 (2025) 3007–3058, https://doi.org/10.1021/acs.chemrev.4c00295.
[58] Y. Deng, X. Wang, H. Liu, H. Cai, C. Song, Y.R. Chi, D. Wei, Z. Jin, N-heterocyclic carbene-catalyzed chemo- and enantioselective three-component esterification/amidation relay for access to planar chiral ferrocene derivatives, ACS Catal. 15 (2025) 6130–6140, https://doi.org/10.1021/acscatal.4c07576.
[59] A.A.J. Torriero, Harnessing ferrocene for hydrogen and carbon dioxide transformations: from electrocatalysis to capture, Inorganics 13 (2025) 244, https://doi.org/10.3390/inorganics13070244.
[60] Y.-C. Kao, M.G. Mohamed, P.-H. Chen, A.A. Thabet, A.A.K. Mohammed, S.-W. Kuo, Characterization and polymerization kinetics of triazine-based benzoxazine monomers: effects of pyridine and bromine interactions, ACS Appl. Polym. Mater. 7 (2025) 10212–10223, https://doi.org/10.1021/acsapm.5c02017.
[61] M.M. Samy, S.U. Sharma, M.G. Mohamed, A.A.K. Mohammed, S.V. Chaganti, J.-T. Lee, S.-W. Kuo, Conjugated microporous polymers containing ferrocene units for high carbon dioxide uptake and energy storage, Mater. Chem. Phys. 287 (2022) 126177, https://doi.org/10.1016/j.matchemphys.2022.126177.
[62] M.M. Samy, M.G. Mohamed, S.-W. Kuo, Conjugated microporous polymers based on ferrocene units as highly efficient electrodes for energy storage, Polymers 15 (2023) 1095, https://doi.org/10.3390/polym15051095.
[63] X. Zhao, Y. Qi, J. Li Q, Porous organic polymers derived from ferrocene and tetrahedral silicon-centered monomers for carbon dioxide sorption, Polymers 14 (2022) 370, https://doi.org/10.3390/polym14030370.
[64] Z. Tan, H. Su, Y. Guo, H. Liu, B. Liao, A.M. Amin, Q. Liu, Ferrocene-based conjugated microporous polymers derived from yamamoto coupling for gas storage and dye removal, Polymers 12 (2020) 719, https://doi.org/10.3390/polym12030719.
[65] Y. Wang, Y. Yang, Q. Deng, W. Chen, Y. Zhang, Y. Zhou, Z. Zou, Recent progress of amorphous porous organic polymers as heterogeneous photocatalysts for organic synthesis, Adv. Funct. Mater. 33 (2023) 2307179, https://doi.org/10.1002/adfm.202307179.
[66] D. Liu, F. Qiu, N. Liu, Y. Cai, Y. Guo, B. Zhao, Y. Qiu, Pore structure characterization and its significance for gas adsorption in coals: a comprehensive review, Unconv. Resour. 2 (2022) 139–157, https://doi.org/10.1016/j.uncres.2022.10.002.
[67] M.G. Mohamed, C.C. Chen, S.W. Kuo, Nitrogen and sulfur co-doped microporous carbon through benzo[c]-1,2,5-thiadiazole-functionalized benzoxazine-linkage porous organic polymer in CO_2 capture and energy storage, React. Funct. Polym. 214 (2025) 106286, https://doi.org/10.1016/j.reactfunctpolym.2025.106286.
[68] X. Fu, Y. Zhang, S. Gu, Y. Zhu, G. Yu, C. Pan, Z. Wang, Y. Hu, Metal microporous aromatic polymers with improved performance for small gas storage, Chem. A Eur. J. 21 (2015) 13357–13363, https://doi.org/10.1002/chem.201501594.
[69] M.G. Kotp, S.-W. Kuo, Selective capturing of the CO_2 emissions utilizing ecological (3-mercaptopropyl)trimethoxysilane-coated porous organic polymers in composite materials, Polymers 16 (2024) 1759, https://doi.org/10.3390/polym16131759.
[70] M.G. Mohamed, A.M. Elewa, N.P. Chen, A.A.K. Mohammed, S.W. Kuo, Construction of malononitrile-functionalized conjugated microporous COFs as adsorbents for effective adsorption of rhodamine B and density functional theory perspective, Colloids Surf. A Physicochem. Eng. Asp. 721 (2025) 137214, https://doi.org/10.1016/j.colsurfa.2025.137214.
[71] D.C. Webster, Cyclic carbonate functional polymers and their applications, Prog. Org. Coat. 47 (2003) 77–86, https://doi.org/10.1016/S0300-9440(03)00074-2.
[72] L. Guo, K.J. Lamb, M. North, Recent developments in organocatalysed transformations of epoxides and carbon dioxide into cyclic carbonates, Green Chem. 23 (2021) 77–118, https://doi.org/10.1039/D0GC03465G.
[73] Q. Cheng, T. Liu, T. Zhao, Targeted weaving of triazine ionic polymers within the pores of covalent organic frameworks for enhanced CO_2 conversion, Langmuir 41 (2025) 29278–29287, https://doi.org/10.1021/acs.langmuir.5c03978.
[74] J. Zhao, X. Yan, X. Liu, Y. Zhang, F. Li, S. Li, Y. Hao, Z. Zhu, T. Chang, B. Wu, Construction on ferrocene-derived imidazole ionic polymers for carbon dioxide cycloaddition and iodine capture, J. Environ. Chem. Eng. 13 (2025) 115695, https://doi.org/10.1016/j.jece.2025.115695.